

Search of Intermediate Mass Black Holes at Low Redshift with Intra-night Variability

LAEL SHIN,¹ JONG-HAK WOO,^{1,2} DONGHOON SON,¹ HOJIN CHO,¹ TAEWOO KIM,³ ELENA GALLO,⁴ AND WONSEOK KANG³

¹*Department of Physics & Astronomy, Seoul National University, Seoul 08826, Republic of Korea*

²*SNU Astronomy Research Center, Seoul National University, Seoul 08826, Republic of Korea*

³*National Youth Space Center, Goheung 59567, Republic of Korea*

⁴*Department of Astronomy, University of Michigan, 1085 S University Ave, Ann Arbor, MI 48109, USA*

ABSTRACT

We present a sample of intermediate-mass black hole (IMBH) candidates based on the detection of a broad H α emission line and variability, which are selected from the Sloan Digital Sky Survey Data Release 7. By performing spectral decomposition of emission lines as well as visual inspection, we initially identified 131 targets with a broad H α line among a large sample of emission-line galaxies. We further selected 25 IMBH candidates, whose estimated black hole mass (M_{BH}) is less than $10^6 M_{\odot}$. To constrain the nature of these candidates, we analyzed X-ray properties and performed an intra-night variability monitoring with optical telescopes. Based on the optical variability analysis, we report a sample of 11 targets with detected intra-night variability as the best IMBH candidates, which are suitable for follow-up observations for accurate M_{BH} determination such as reverberation mapping campaigns.

Keywords: galaxies: active — galaxies: nuclei — techniques: photometric

1. INTRODUCTION

The decades-long observations have established that supermassive black holes (SMBHs) with mass $>10^6 M_{\odot}$ are universal in the center of massive galaxies at low redshift (e.g., see Kormendy & Richstone 1995; Kormendy & Ho 2013), yet the origin and the mass range of the high-redshift seeds of these SMBHs are unclear. The existence of stellar mass black holes (BHs) in a much lower mass range $\sim 10\text{-}100 M_{\odot}$ has been well studied by various observations of electromagnetic radiation as well as gravitational wave (e.g., Remillard & McClintock 2006; Thompson et al. 2019; Abbott et al. 2020). However, discovery of $\sim 10^9 M_{\odot}$ SMBH in the very early universe triggered a fundamental question on the BH formation and seed mass (Mortlock et al. 2011; Bañados et al. 2018; Onoue et al. 2019). One of the scenarios suggests that the progenitor of the high- z SMBHs is much heavier than normal stellar mass BH (e.g., Loeb & Rasio 1994; Latif et al. 2013; Greene et al. 2020).

Thus, by bridging the two well-observed M_{BH} ranges, systematic search of intermediate-mass black holes

(IMBHs) with masses of $10^3 - 10^6 M_{\odot}$ in the present-day universe is pivotal to understand how the seeds of SMBH formed and evolved throughout cosmic time (e.g., Volonteri et al. 2008; Greene 2012; Greene et al. 2020). If some of the seed BHs at high redshift remain as IMBHs without significantly growing over cosmic time, the relics of the seed can be observed in nearby galaxies as IMBHs (e.g., Greene 2012; Reines & Comastri 2016; Mezcua 2017; Woo et al. 2019a).

Nevertheless, IMBHs are rarely observed, hence, they are called the ‘missing link’ between stellar mass BHs and SMBHs (see review by Mezcua 2017). The evidence of IMBH candidates has been found from various observations. First, X-ray emission and the dynamical modeling of a number of globular clusters (GCs) suggested the presence of an IMBH in their center (e.g., Gebhardt et al. 2000; Gerssen et al. 2002; Pooley & Rappaport 2006). For example, Silk & Arons (1975) first argued that the X-ray flux from their GC targets could be explained by the accretion of the IMBHs with masses in the range $100\text{-}1000 M_{\odot}$. Baumgardt (2017) also claimed that IMBH with mass of $\sim 4 \times 10^4 M_{\odot}$ exists in ω Centauri by analyzing the velocity dispersion profile of the stars in the GC. Tens of IMBH candidates were identified in similar ways, but their methodologies depended on the complicated models of kinematics and radiation,

limited to nearby IMBH candidates. Second, extragalactic ultra-luminous X-ray sources (ULXs) were proposed as IMBHs. Black hole mass estimation based on the fundamental plane of accreting black holes (e.g., Webb et al. 2012; Cseh et al. 2015) and the X-ray spectrum fitting (e.g., Miller et al. 2003; Sutton et al. 2012) indicated that several BHs were in the IMBH mass range. These methods required multi-wavelength observations, including X-ray and radio, along with complex modeling of the accretion disk.

Detection of the broad emission lines, which are one of the main signatures of mass-accreting type 1 active galactic nuclei (AGN), also provided evidence for IMBH candidates (e.g., Filippenko & Ho 2003; Greene & Ho 2004, 2007; Dong et al. 2012). Compared with the other methods, this method enables discovery of IMBH candidates in distant galaxies, and the mass of these candidates can be better determined. Assuming that the gas in the broad line region (BLR) is virialized and governed by the gravitational potential of the central black hole, the mass of the black holes can be determined based on the virial relation:

$$M_{BH} = f \times R_{BLR} \Delta V^2 / G \quad (1)$$

where R_{BLR} is the BLR size, ΔV is the velocity of gas measured from the width of broad emission lines, and f is a dimensionless scale factor depending on the kinematics and geometry of the BLR (e.g., Peterson 1993; Peterson et al. 2004). Adopting the correlation between AGN continuum luminosity (or emission line luminosity) and the BLR size (e.g., Bentz et al. 2013), the black hole mass can be indirectly estimated based on single-epoch spectra (e.g., Woo & Urry 2002; Greene & Ho 2005; Park et al. 2012; Shen & Liu 2012; Le et al. 2020).

Among the broad emission lines, the $H\alpha$ line is often utilized to identify type 1 AGNs because of its high intensity (e.g., Woo et al. 2014; Eun et al. 2017). While typical type 1 AGNs with strong $H\alpha$ have M_{BH} larger than $10^6 M_{\odot}$, a relatively weak broad $H\alpha$ line should be present in AGNs with intermediate-mass. Thus, a number of studies utilized the presence of a weak broad $H\alpha$ to search IMBH (e.g., Greene & Ho 2004, 2007; Dong et al. 2012; Reines et al. 2013; Liu et al. 2018; Chilingarian et al. 2018).

For example, Reines et al. (2013) identified IMBH candidates by detecting a weak broad component of the $H\alpha$ emission line, using a sample of galaxies at $z < 0.055$, whose stellar mass is smaller than $3 \times 10^9 M_{\odot}$ by assuming that IMBHs are more likely to exist in dwarf galaxies as suggested by black hole mass - stellar mass relation (e.g., Greene 2012; McConnell & Ma 2013; Reines & Comastri 2016). Based on the broad $H\alpha$, they reported

17 IMBH candidates, however, additional studies are required to confirm their mass because the mass estimation based on the single-epoch spectrum analysis suffers from large uncertainty, and it is possible that other sources such as luminous blue variable stars may be responsible for the broad $H\alpha$ (e.g., Izotov & Thuan 2007, 2009a).

The true nature of IMBH candidates can be constrained by other properties of type 1 AGNs. For example, detection of the high-luminosity of X-ray emission can provide a constraint to confirm whether they are mass-accreting BHs since AGNs are sources of strong X-ray radiation (e.g., Elvis et al. 1978; Nucita et al. 2017; Chilingarian et al. 2018; Liu et al. 2018). Variability also provides strong constraints as the AGN continuum and emission line flux changes over time (e.g., Rodríguez-Pascual et al. 1997; Walsh et al. 2009; Rakshit & Stalin 2017; Baldassare et al. 2018; Martínez-Palomera et al. 2020). In the case of IMBH, variability test over intra-night or several day time scale is a crucial tool for identification of these candidates (e.g., Mushotzky et al. 2011; Aranzana et al. 2018; Kim et al. 2018).

In this paper we present the results of our systematic search of IMBH candidates. By detecting the $H\alpha$ emission line and focusing on the targets with the weakest $H\alpha$ broad component, we identified a sample of IMBH candidates. Then, we investigated X-ray properties and intra-night variability. We describe sample selection in Section 2, observations and the data reduction in Section 3, and variability analysis in Section 4. We provide discussion in Section 5, and summary and conclusion are followed in Section 6.

2. SAMPLE SELECTION

2.1. Local AGN & Star-forming Galaxy Sample

To find IMBH candidates by detecting a weak $H\alpha$ broad component, we started with a large sample of emission line galaxies from Bae & Woo (2014) and Woo et al. (2016), who classified 60,018 type2 AGN-host galaxies and 128,951 star-forming galaxies (SFGs) based on the flux ratios of the emission lines (Kauffmann et al. 2003), using the Max Planck institute for astrophysics and the Johns Hopkins university (MPA-JHU) catalog of SDSS DR7 galaxies (Abazajian et al. 2009). For robust spectral analysis, they restricted the sample with two criteria: (1) signal-to-noise ratio (S/N) > 3 for the four emission lines, $H\beta$, [OIII] $\lambda 5007$, $H\alpha$, and [NII] $\lambda 6584$; (2) amplitude(peak)-to-noise ratio (A/N) > 5 for both $H\alpha$, and [OIII] $\lambda 5007$ emission lines. Based on these criteria, we selected 10,958 type 2 AGNs at $z < 0.1$. We also obtained 22,000 SFGs at $z < 0.1$ by limiting stellar mass of the host galaxy $M_{*} < 10^{10} M_{\odot}$, in order

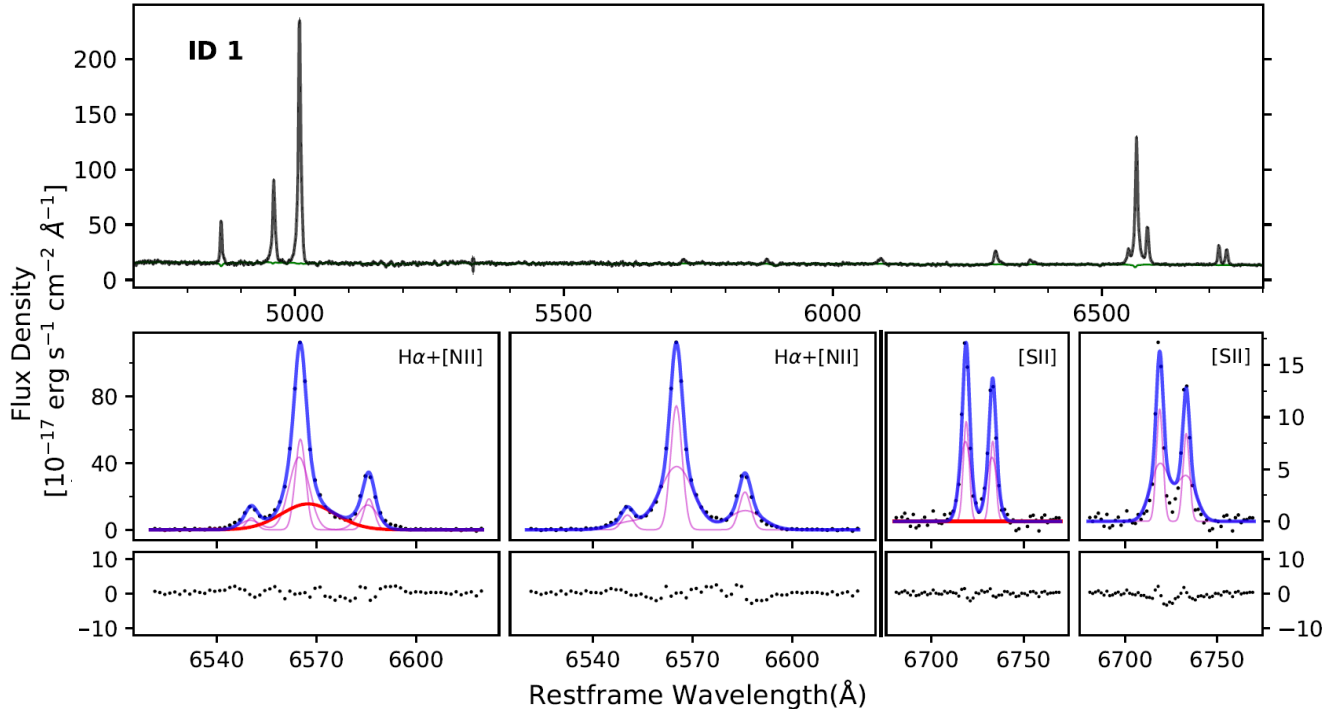


Figure 1. Example of a broad H α candidate (ID 1) whose estimated M_{BH} is smaller than $10^6 M_{\odot}$. The top panel shows the redshift-corrected spectrum with the best stellar continuum fit plotted in green. In the bottom panels, the first and third column show the best fit model with H α broad component for each emission line region. The second and fourth column show the best fit model without H α broad component. The stellar continuum subtracted spectrum is plotted black, and the blue line shows the best fit model composed of narrow Gaussian components (magenta) and H α broad component (red). At the bottom of each panel, the residuals between the spectrum and the best fit model are plotted in black. Spectra of the other 24 broad H α candidates with estimated $M_{\text{BH}} < 10^6 M_{\odot}$ are shown in the Appendix.

to survey dwarf galaxies, which are more likely to host IMBHs (e.g., McConnell & Ma 2013; Reines & Comastri 2016).

2.2. IMBH candidates with a Broad H α Component

2.2.1. Spectral decomposition

We performed spectral decomposition to investigate the presence of a broad H α component using the selected AGNs and SFGs. It is crucial to decompose AGN emission lines from the host galaxy stellar continuum for properly measuring the flux and velocity dispersion of H α . We first subtracted the stellar continuum from the SDSS spectra by using the penalized pixel-fitting (pPXF) routine (Cappellari & Emsellem 2004), which finds the best-fit stellar template for the given galaxy spectra. For this process, we used MILES simple stellar population models with solar metallicity (Sánchez-Blázquez et al. 2006). Before the fitting process, we masked the optical emission lines and the H α emission line region (i.e., 6300-6900Å) to prevent fitting a potential broad emission line as a stellar continuum. We then subtracted the best-fit continuum model from the observed spectra, leaving the pure emission line spectra.

Then, we constructed the emission line model for the region around H α (i.e., 6400-6800Å), where [NII] λ 6548, [NII] λ 6584, [SII] λ 6717, and [SII] λ 6731 lines are also located. To confirm the presence of a broad H α component, we used four different fitting schemes: (a) which fit the narrow component of each emission line ([NII], [SII], and H α) with a single Gaussian model, without including an additional Gaussian model for a potential broad H α line, (b) which fit the narrow component with a double Gaussian model without including an additional broad H α component, (c) which fit the narrow component with a single Gaussian model and add one more Gaussian model for a broad H α line, (d) which fit the narrow component with a double Gaussian model and include an additional model for a broad H α line. We fixed the relative separations between the centers of each emission line model to the laboratory value, and the width of each narrow emission line to the equal value assuming that they are emitted from the cloud with the same kinematical properties. Furthermore, in the double Gaussian model for narrow components, we added a constraint that the amplitude ratio of the two Gaus-

Table 1. X-ray detected broad H α candidates

SDSS Name	Mission	E range	$\log F_{X-ray}$	Distance	$\log L_{X-ray}$	$\log L_{H\alpha}$	$\log M_{BH}$
(1)	(2)	(3)	(4)	(5)	(6)	(7)	(8)
J075953.48+232324.2	XMM-Newton	0.2-12	-11.0	132	43.3	40.2	6.1
J083736.97+245959.2	XMM-Newton	0.2-12	-13.2	131	41.1	39.9	6.1
J084344.98+354942.0	Swift	15-150	-11.0	241	43.9	41.0	6.2
J090229.38+032305.9	Chandra	0.3-8.0	-12.8	124	41.5	39.9	6.2
J094319.14+361452.1	ROSAT	0.1-2.4	-12.5	102	41.6	40.2	6.4
J110306.23+554100.0	ROSAT	0.1-2.4	-12.4	217	42.3	40.2	6.5
J110501.97+594103.6	Chandra	0.3-8.0	-11.9	151	42.6	40.8	6.7
J112301.31+470308.6	XMM-Newton	0.2-12	-14.0	114	40.2	40.0	6.1
J114612.17+202329.9	Chandra	0.3-8.0	-11.9	108	42.2	40.4	6.4
J133514.41+104110.2	XMM-Newton	0.2-12	-11.7	180	42.9	40.4	6.7
J134632.13+642325.1	XMM-Newton	0.2-12	-11.0	108	43.2	40.3	6.3
J135419.95+325547.7 ^a	XMM-Newton	0.2-12	-11.2	118	43.0	40.7	6.8
	Chandra	0.3-8.0	-12.0		42.2		
J141451.34+030751.3	Einstein	0.2-4	-12.6	115	41.6	40.0	6.2
J143318.47+344404.4	Chandra	0.3-8.0	-12.5	154	42.0	40.2	6.5
J143642.70+341837.5	Chandra	0.3-8.0	-13.4	197	41.2	39.9	6.2
J144108.69+351958.8	ASCA	0.7-7	-12.4	352	42.8	40.9	6.3
J144958.69+522801.3	ROSAT	0.1-2.4	-13.1	421	42.2	40.9	6.4
J151405.52+094209.7	ROSAT	0.1-2.4	-12.8	347	42.3	40.4	6.6
J212512.47-071329.8	Chandra	0.3-8.0	-12.3	280	42.6	40.6	6.6

NOTE—(1) SDSS name. (2) X-ray mission name. (3) Energy range of the X-ray observation in units of keV. (4) Absorption-corrected X-ray flux in units of $\text{erg s}^{-1} \text{cm}^{-2}$. (5) Distance derived from the redshift in units of Mpc. (6) Absorption-corrected X-ray luminosity in units of erg s^{-1} . (7) Luminosity of the H α broad component estimated in this study in units of erg s^{-1} . (8) Black hole mass estimated in this study.

^aObserved in both missions XMM-Newton and Chandra.

sian components should be equal for each emission line model.

For modeling, we used `curve_fit` tool of python `scipy` package (Virtanen et al. 2020), which utilizes trust region reflective algorithm. To evaluate the reliability of the fitting results, we calculated their reduced chi square (χ_{red}^2) and Bayesian information criterion (BIC) as

$$\chi_{red}^2 = \frac{1}{n-m} \sum_i \frac{(O_i - C_i)^2}{\sigma_i^2} \quad (2)$$

$$BIC = \sum_i \frac{(O_i - C_i)^2}{\sigma_i^2} + m \ln n \quad (3)$$

where O_i is the observed flux density at each wavelength, C_i is the model flux density, and σ_i refers to the flux density error. They both consider the number of the data (n) and the number of the model parameters (m). Similar to χ_{red}^2 , a better fitting model has less BIC. However, BIC has a penalty term ($m \ln n$) for the number

of the model parameters, so a more reliable comparison can be done between the models with different number of parameters. When the difference between the BIC values of two models is greater than 10, it is rated as a strong evidence against the significance of the model with higher BIC (Kass & Raftery 1995).

Based on the results, we set the criteria to select the candidates with a broad H α line. To prevent the overfitting problem, we employed single Gaussian model for the narrow component if the BIC of model (a) is less than the BIC of model (b) + 10, if not, used double Gaussian model for the narrow component. We initially selected the candidates which have a broad H α line using criteria as follows.

- velocity dispersion of H α broad component after correcting for the SDSS instrumental resolution (60 km s^{-1}) $> 250 \text{ km s}^{-1}$ (i.e. $\sim 590 \text{ km s}^{-1}$ FWHM)
- A/N of H α broad component > 20 (10 for SFGs)

- BIC of the model with H α broad component + 10 < BIC of the model without H α broad component
- χ_{red}^2 of the model with H α broad component + 10 < χ_{red}^2 of the model without H α broad component

The adopted lower limit of the velocity width (i.e., velocity dispersion 250 km s⁻¹ or FWHM = \sim 590 km s⁻¹) seems lower than the typical definition of the type 1 AGNs (i.e., >1000 km s⁻¹ FWHM; e.g., Vanden Berk et al. (2006)). However, velocity dispersion of 250 km s⁻¹ is much larger than stellar velocity dispersion due to gravitational potential of low-mass galaxies. Instead, the line broadening is likely caused by the gravitation of the central black hole. Thus, we interpreted that the line component broader than 250 km s⁻¹ is originated from the BLR of the central black hole. There is little concern that the narrow and broad component are misclassified since the narrow line of all candidate is much narrower than 250 km s⁻¹. Note that our approach of the velocity lower limit is similar to that of the previous study by Reines et al. (2013), who surveyed IMBH candidates with a lower limit of FWHM = 500 km s⁻¹ (i.e., velocity dispersion of \sim 210 km s⁻¹). In addition, we applied smaller amplitude-to-noise ratio cut (A/N > 10) for SFGs than the A/N of AGNs to include more SFGs. Based on these criteria, we obtained 1,484 type 2 AGNs and 116 SFGs for further analysis.

We visually inspected the spectral decomposition results and the presence of H α broad component for these \sim 1,500 targets. First, we checked the decomposition result without including a broad H α model. If there is no significant residual around the H α and [SII] region, we assume that no broad H α component is present, excluding the target from the candidate list, since it is not clear whether a H α broad component is required in the best-fit model. We present an example of emission line decomposition results with or without a broad H α model in Figure 1. Because the width of each emission line model is held fixed by the same value, the model without a broad H α component makes the [SII] line model much broader than the best-model.

There are also examples of the opposite case shown in the Appendix. If a model without a broad H α model fits the [SII] lines, it makes the H α line model much narrower than the best-model, so a significant residual is present around the H α line. In contrast, the model with a broad H α component fits both [SII] and H α emission line better. Based on the visual inspection, we finalized 738 candidates from type 2 AGNs and 4 candidates from SFGs.

2.2.2. Black hole mass estimation

We estimated black hole mass (M_{BH}) of the sample of 738 type 1 AGNs with a broad H α , to select the IMBH candidates. Note that 611 targets among 738 objects were previously studied by Eun et al. (2017). Since their estimated black hole mass is larger than $10^6 M_{\odot}$, we excluded them from the sample of IMBH candidates. For remaining 131 AGNs, we determine M_{BH} using a single-epoch estimator based on the virial assumption and the BLR size - luminosity (L_{5100}) relation (Bentz et al. 2013). Because the H α luminosity can be used as a proxy of the AGN continuum luminosity (Greene & Ho 2005):

$$L_{H\alpha} = (5.25 \pm 0.02) \times 10^{42} \left(\frac{L_{5100}}{10^{44} \text{ erg s}^{-1}} \right)^{(1.157 \pm 0.005)} \text{ erg s}^{-1}, \quad (4)$$

we determine M_{BH} using the velocity dispersion ($\sigma_{H\alpha}$) and luminosity ($L_{H\alpha}$) of the H α broad component (Woo et al. 2015):

$$M_{BH} = f \times 10^{(6.56 \pm 0.06)} \left(\frac{L_{H\alpha}}{10^{42} \text{ erg s}^{-1}} \right)^{(0.46 \pm 0.03)} \times \left(\frac{\sigma_{H\alpha}}{10^3 \text{ km s}^{-1}} \right)^{(2.06 \pm 0.06)} M_{\odot}, \quad (5)$$

where $\log f = 0.65 \pm 0.12$ is the virial factor.

We determined the error of each model parameter by calculating the square root of the diagonal term of the covariance matrix provided by `curve_fit` tool, and calculated the measurement uncertainty of the M_{BH} using standard propagation of the errors. Considering the intrinsic scatter of the size-luminosity relation (0.19 dex; Bentz et al. 2013) and the uncertainty of the virial factor (0.12 dex; Woo et al. 2015) as systematic uncertainties, we obtained the total error of M_{BH} by adding the measurement and systematic uncertainties in quadrature. The combined error is typically \sim 0.24 dex.

In Figure 2, we present the distribution of the H α luminosity, velocity dispersion and M_{BH} of the 131 type 1 AGNs. The estimated M_{BH} is in the range $\sim 10^{5.3} - 10^{7.2} M_{\odot}$ with a median of $10^{6.3} M_{\odot}$, while we found no target with $M_{BH} < 10^5 M_{\odot}$. Among them, we identified 25 targets with $M_{BH} < 10^6 M_{\odot}$ as IMBH candidates.

2.3. X-ray black hole candidates

To find additional evidences that the selected 131 targets with a broad H α line are AGNs, we investigated X-ray properties by retrieving the X-ray flux data from the online archive NASA/IPAC Extragalactic Database¹

¹ <https://ned.ipac.caltech.edu/>

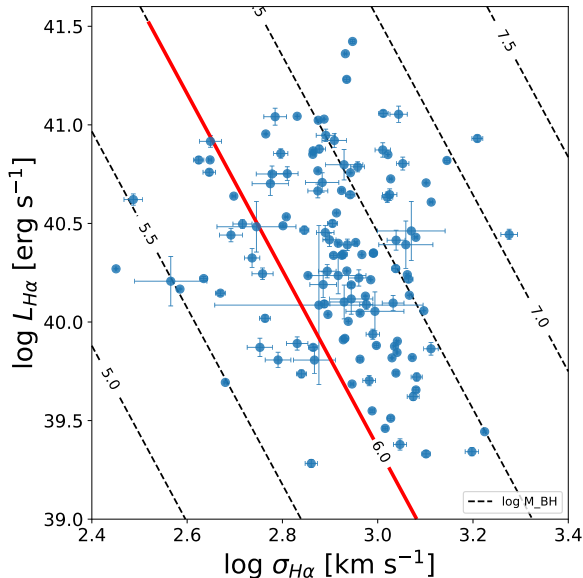


Figure 2. Luminosity and velocity dispersion of the H α broad component for the 131 broad H α candidates. Slanted black lines are equi- M_{BH} lines. Red line is the selection criteria, $10^6 M_{\odot}$, for the IMBH candidates.

and NASA HEASARC Xamin Web interface². For 19 targets we obtained X-ray flux data between 0.1 and 150 keV using archival data of various X-ray missions (see Table 1). The measured X-ray luminosity ranges from $\sim 10^{40}$ to 10^{44} erg s $^{-1}$ with a median luminosity of $\sim 10^{42.3}$ erg s $^{-1}$. However, the estimated M_{BH} of these targets are larger than $10^6 M_{\odot}$, resulting in no IMBH candidate with available X-ray luminosity. Note that the targets with M_{BH} close to $10^6 M_{\odot}$ can be IMBHs if

we consider relatively large uncertainty of the estimated M_{BH} .

2.4. Pilot sample for a variability test

Using the selected 25 IMBH candidates, we performed optical variability test in order to confirm them as AGNs. In addition, we also observed the IMBH candidates from Reines et al. (2013) as complementary candidates, for which no optical variability test has been performed by Reines et al. (2013). By applying the same criteria ($M_{\text{BH}} < 10^6 M_{\odot}$) to the sample of Reines et al. (2013), we found 16 targets as a IMBH candidate. Only one target is overlapped with our sample of 25 objects. Note that there are difference between the work of Reines et al. (2013) and ours due to the details of the spectral decomposition. Unlike this study, for example, they subtracted the stellar continuum using different stellar model templates from Tremonti et al. (2004), and fitted [SII] and H α + [NII] composite separately. In addition, they only used the reduced χ^2 to evaluate the spectral decomposition results. The fitting range, fixed parameters for the emission line model, stellar mass limit (i.e., $< 3 \times 10^9 M_{\odot}$) and the redshift range ($z < 0.055$) are also different. Excluding this one overlapped target, we finalized a sample of 40 IMBH candidates for the variability test observations.

To setup monitoring strategy, we estimated the expected time lag between AGN continuum and H α emission line (τ) based on the BLR size - luminosity relation (Bentz et al. 2013), after adopting the H α luminosity as a proxy of continuum luminosity (Equation 4). The estimated time lag ranges from 0.3 to 5.3 days with a median of 1.9 days. We assign a priority to the candidates with a shorter time lag since they are more likely to have lower M_{BH} .

² <https://heasarc.gsfc.nasa.gov/xamin/>

Table 2. Observation information of the observed sample

ID	NSAID	RA	Dec	z	Filter_cont	Filter_H α	Date (yy.mm.dd)	Exp_time (cont./H α)	# epoch (cont./H α)	Observatory	Reference
(1)	(2)	(3)	(4)	(5)	(6)	(7)	(8)	(9)	(10)	(11)	(12)
1	10779	09:06:13.8	+56:10:15.2	0.047	kp1494	kp1517	20.01.08	600/600	4/4	MDM	This study
3	33430	08:07:07.2	+36:14:00.5	0.032	kp1494	kp1497	20.01.04	600/600	5/5	MDM	This study
4	17134	09:55:40.5	+05:02:36.7	0.034	kp1494	kp1497	20.01.08	600/600	3/3	MDM	This study
5 ^a	33232	13:08:41.7	+52:46:27.4	0.024	V	R	20.05.13	840/840	4/4	DOAO	This study
					V	kp1496	21.06.25	360/900	4/4	MDM	
8	116134	09:14:24.8	+11:56:25.6	0.031	kp1494	kp1497	20.01.08	600/600	4/4	MDM	This study
9 ^a	45989	16:29:38.4	+38:41:39.3	0.036	V	R	20.06.01	840/840	5/5	DOAO	This study
					V	kp1497	21.06.29	360/720	3/4	MDM	
11	59182	10:29:11.5	+39:06:53.6	0.026	kp1494	kp1496	20.01.08	600/600	4/4	MDM	This study
14 ^a	125613	16:24:51.3	+19:25:35.7	0.036	V	R	20.06.01	840/840	5/5	DOAO	This study
					V	kp1497	21.08.02	360/600	4/4	MDM	
20	15709	08:04:31.1	+40:12:21.8	0.040	kp1494	kp1498	20.01.04	600/600	6/6	MDM	This study
23	9576	08:01:42.6	+42:00:19.5	0.032	kp1494	kp1497	20.01.04	600/600	6/6	MDM	This study
27	125318	09:54:18.2	+47:17:25.2	0.033	V	kp1497	20.02.15	360/1200	5/5	MDM	RGG
29 ^a	18913	15:34:25.6	+04:08:06.7	0.040	V	R	20.06.07	840/840	3/3	DOAO	RGG
					V	kp1498	21.06.28	360/900	4/4	MDM	
30	109016	10:14:40.2	+19:24:49.0	0.029	V	kp1496	20.03.04	360/1200	4/4	MDM	RGG
31	12793	10:51:00.7	+65:59:40.5	0.033	V	kp1497	20.03.04	360/1200	4/4	MDM	RGG
32	91579	12:03:25.7	+33:08:46.2	0.035	V	kp1497	20.03.04	360/1200	5/5	MDM	RGG
34 ^a	99052	16:05:31.9	+17:48:26.2	0.032	V	R	20.06.07	840/840	3/3	DOAO	RGG
					V	kp1497	21.08.02	360/600	4/4	MDM	
35	112250	11:23:15.8	+24:02:05.2	0.025	V	kp1496	20.03.04	360/1200	4/4	MDM	RGG
36	47066	08:51:25.8	+39:35:41.8	0.041	V	kp1498	20.02.15	360/1200	4/5	MDM	RGG
38 ^a	104565	13:43:32.1	+25:31:57.7	0.029	V	R	20.05.13	840/840	4/4	DOAO	RGG
					V	kp1496	21.06.25	360/900	3/3	MDM	
40 ^a	79874	15:26:37.4	+06:59:41.7	0.038	V	R	20.06.07	840/840	3/3	DOAO	RGG

Table 2 *continued*

Table 2 (*continued*)

ID	NSAID	RA	Dec	z	Filter_cont	Filter_H α	Date (yy.mm.dd)	Exp_time (cont/H α)	# epoch (cont./H α)	Observatory	Reference
(1)	(2)	(3)	(4)	(5)	(6)	(7)	(8)	(9)	(10)	(11)	(12)
		V			kp1497	21.06.28	360/900	5/5	MDM		

NOTE—(1) Identification number assigned in this study. (2) NASA-Sloan Atlas identification number. (3) Right Ascension in J2000.0. (4) Declination in J2000.0. (5) Redshift. (6) Filter for the continuum part observation. (7) Filter for the H α part observation. (8) Observation date. (9) Exposure time in units of s for the continuum part and H α part observation. (10) The number of the epochs for the continuum part and H α part observation. (11) Observation site. (12) Name of the original sample. This study: IMBH candidates identified in this study. RGG: IMBH candidates selected from Reines et al. 2013.
^aTargets observed at both observatories.

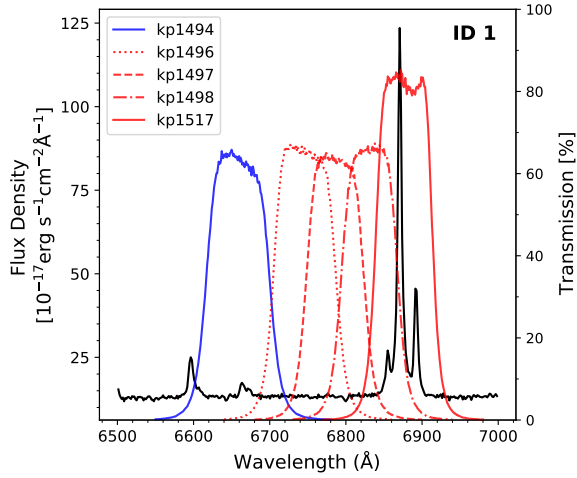


Figure 3. Response function of the selected filters. As an example, the SDSS spectrum of ID1 is plotted (black) along with the kp1494 filter for obtaining continuum flux (blue) and the kp1517 filter for H α . The response function of three additional filters (kp1496, kp1497, and kp1498) are also presented. Note that depending on the redshift of each target, we used a different set of filters.

3. OBSERVATION AND DATA REDUCTION

3.1. Observations

For an intra-night variability test we observed 20 targets out of 40 IMBH candidates in 2020 and 2021. These targets have expected time lag < 2.4 days, and they were observable during our monitoring runs. In 2020, from 4th January to 7th June, we observed 13 targets using the 1.3m telescope at the Michigan-Dartmouth-MIT (MDM) observatory on Kitt peak, Tucson, Arizona, USA, with the Templeton CCD, which has $1K \times 1K$ pixels with a $0.51''$ pixel size and a $8.49' \times 8.49'$ field of view (FOV). The remaining 7 targets were observed with the 1m telescope at the Deokheung optical astronomical observatory (DOAO) in Jeollanam-do, Korea. We used $4K \times 4K$ FLI CCD with 2×2 pixel binning, which provided $0.46''$ pixel size and a $15.8' \times 15.8'$ FOV. In addition, we repeated photometry observations for these 7 objects at the MDM observatory in order to obtain narrow-band filter observations, which were not possible at DOAO due to the lack of narrow filters. More details of the observing facilities can be found in our on-going monitoring studies (e.g., Woo et al. 2019b).

To investigate the variability, we targeted 2-4 candidates in each night and carried out repeated observations of 3-6 epochs with a ~ 1 -2 hours cadence. Among available filters, we used two filters: one filter is selected for obtaining continuum flux without including the H α emission line, and the other filter is set for the H α emission line (see Figure 3). Table 2 lists the observational

details of individual targets, which are sorted by their M_{BH} .

3.2. Data reduction

The standard image preprocess was carried out using the data reduction routine of the Seoul National University AGN monitoring project (SAMP) (Woo et al. 2019b; Rakshit et al. 2019) as outlined below. First, we performed dark, bias image subtraction and flat-fielding using IRAF routines (Tody 1986). We then removed cosmic rays using LA-cosmic (van Dokkum 2001), and derived the astrometric solution with astrometry-net (Lang et al. 2010). Utilizing the solution, we combined the preprocessed exposures of each target using SWarp (Bertin et al. 2002) with a median combine method for a deeper single image. Finally, to match the seeing conditions of individual epochs, we performed seeing convolution with `psf` tool of python `photutil` package and `convolution` tool of python `astropy` package (Astropy Collaboration et al. 2013; Astropy Collaboration et al. 2018). The preprocessed images of 20 observed candidates are presented in Figure 4.

3.3. Differential photometry

We performed differential photometry using the preprocessed images as we aim at detecting flux variation for this study. To determine the optimal aperture size for the photometry, we utilized a star in the image brighter than the target, and determined the aperture size for obtaining the highest S/N. We employed the same aperture for all epochs as seeing of each image was already matched. The typical seeing was FWHM $\sim 3.3''$ at DOAO and $\sim 2.8''$ at MDM in 2020, and $\sim 2.2''$ at MDM in 2021. We adopted an aperture size $\sim 9''$ for both MDM and DOAO data, which roughly corresponds to ~ 3 times of the seeing size.

We measured the instrumental magnitude of each object in the FOV with SExtractor (Bertin & Arnouts 1996), and constructed the differential light curves utilizing 5 comparison stars. To select the non-variable comparison stars, we first selected 20 brightest stars in the image and performed a variability test. We calculated the magnitude difference (Δmag) by subtracting the magnitude of the first epoch from the magnitude of each epoch for individual stars. Then, we determined the error weighted average and standard deviation of Δmag . Based on this calculation, we excluded the stars whose Δmag is larger than the average by more than a factor of two of the standard deviation. After that we tested each case by randomly selecting 5 stars from the remaining comparison stars and picked a set of 5 stars, whose standard deviation of their Δmag is the smallest.

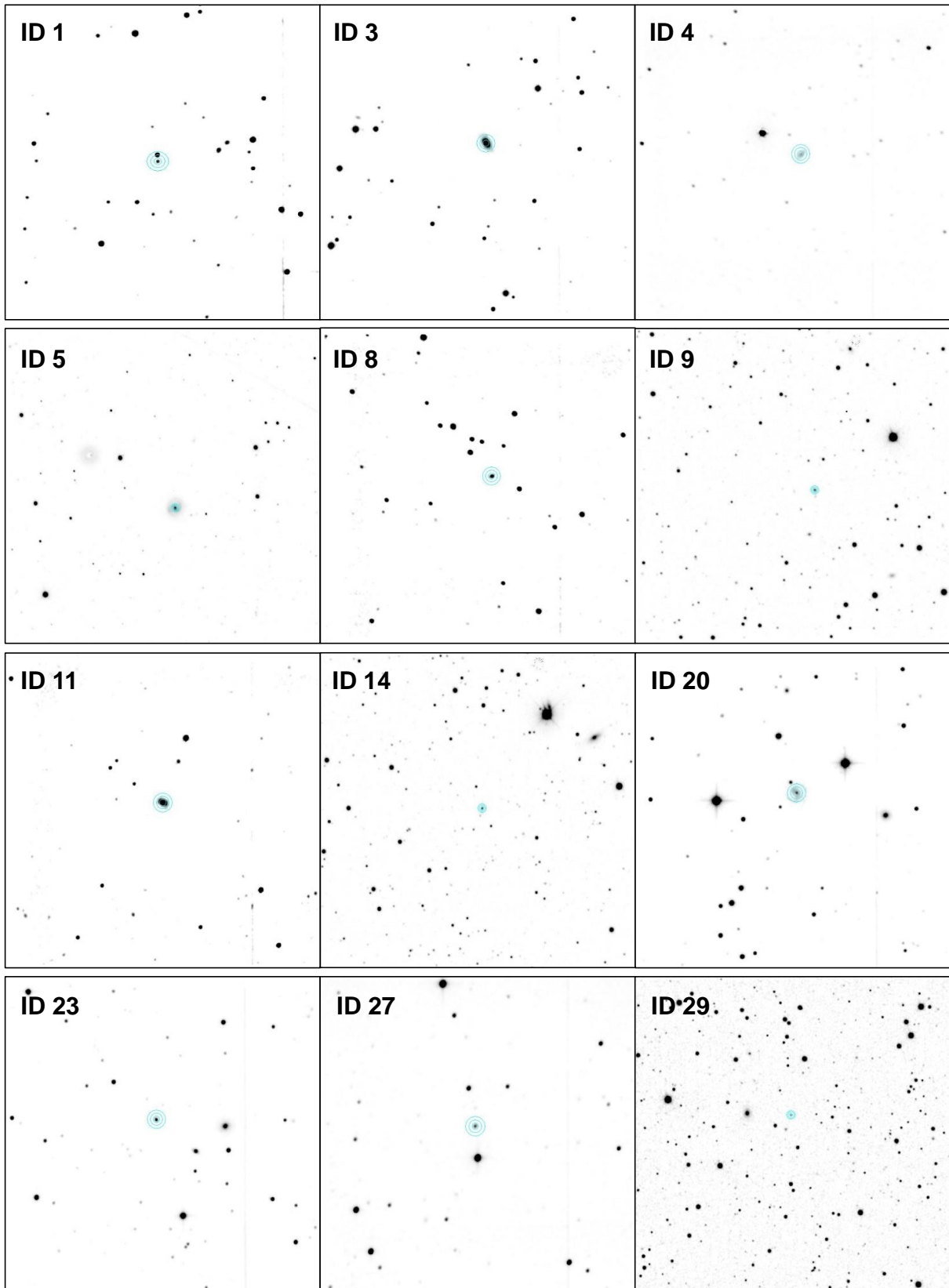


Figure 4. Images of the 20 candidates observed with the $H\alpha$ focused filter (see Table 2). The upper direction is the north, and the left is the east. The 5", 10", 15" apertures are denoted with cyan circles. The ID assigned in this study is shown in the upper left corner of each panel.

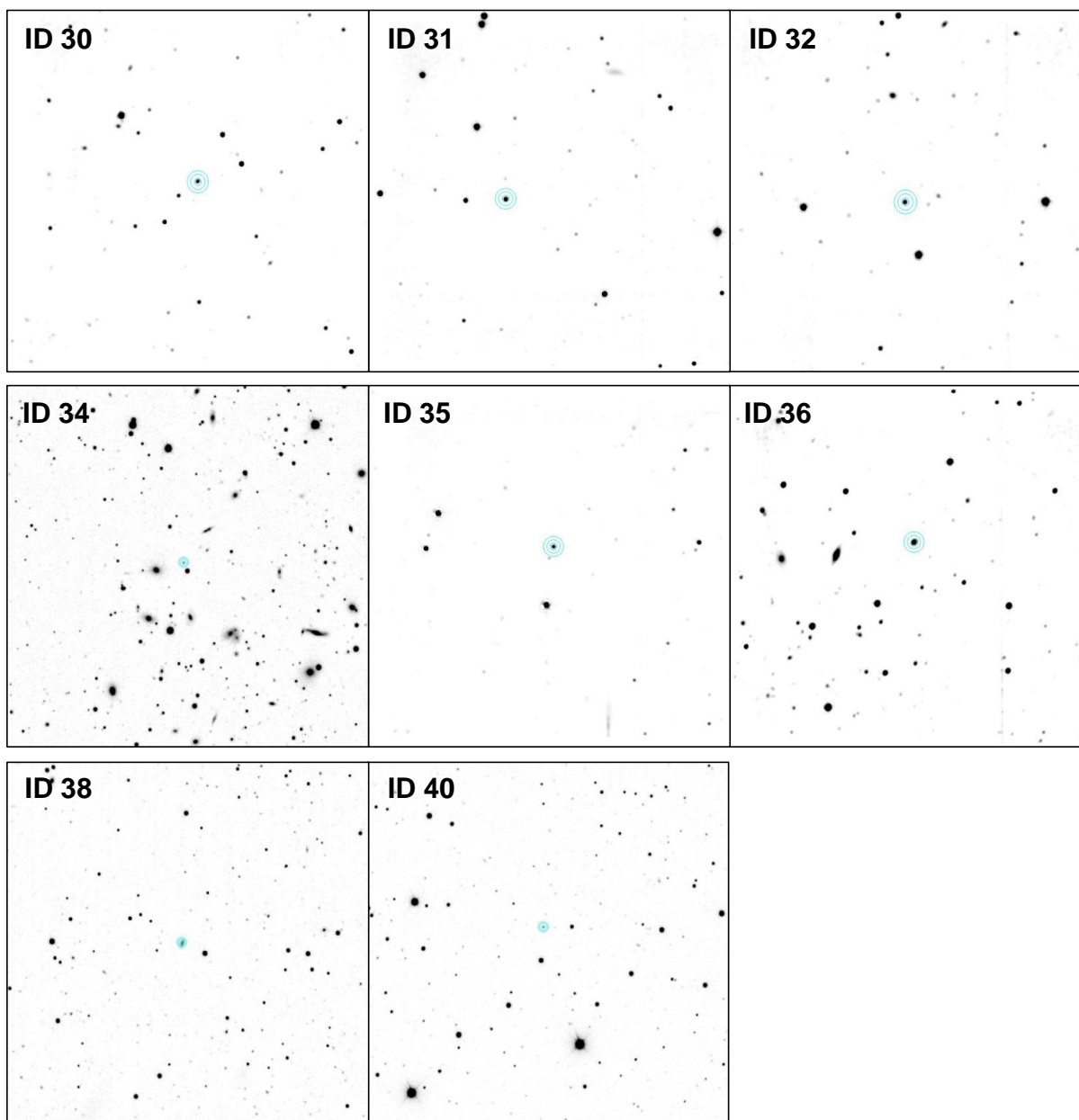


Figure 4. Continued

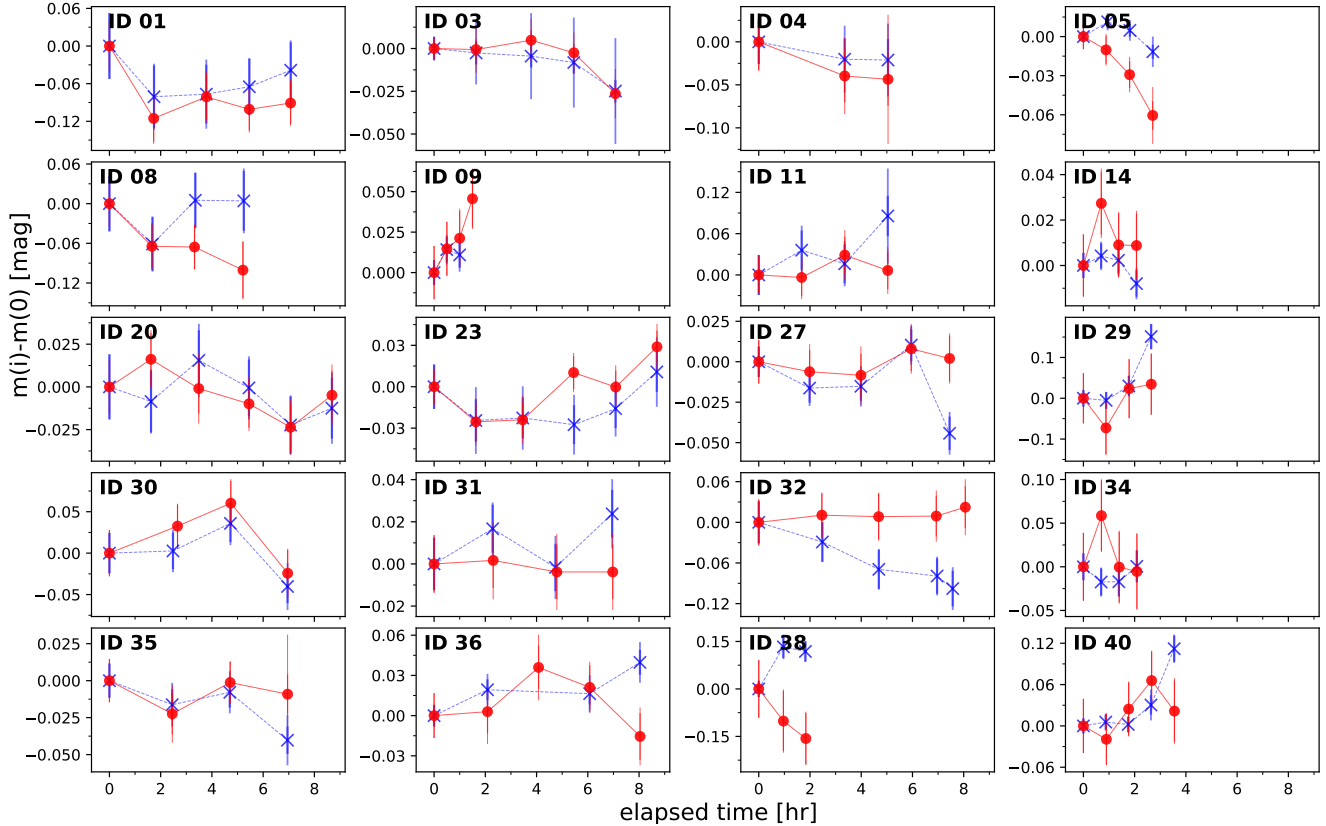


Figure 5. Continuum (blue) and H α (red) light curves of the 20 candidates. The total error (thin line) is composed of measurement error (thick line) and the systematic error from differential photometry. Note that for H α light curves, we only present the photometry results with narrow-band filters. The ID assigned in this work is shown in the upper left corner of the panel.

To estimate the uncertainty of the calibrated magnitude in the light curves, we combined the measurement error (σ_m) and the standard deviation of the Δmag of the selected 5 comparison stars (σ_s) in quadrature:

$$\sigma = \sqrt{\sigma_m^2 + \sigma_s^2}. \quad (6)$$

The calibrated light curves from differential photometry are presented in Figure 5.

4. RESULTS AND ANALYSIS

4.1. Variability amplitude

To investigate the variability of the observed IMBH candidates, we calculated three different parameters, namely, the flux ratio between the maximum and minimum brightness (R_{max}), standard deviation of the magnitudes in the light curve (RMS), and the normalized excess variance of the flux (F_{var}) defined as

$$F_{var} = \frac{\sqrt{f_\sigma^2 - f_\delta^2}}{f_{avg}} \quad (7)$$

where f_{avg} is the average of the flux of the target, f_σ is the standard deviation of the flux, and f_δ is the average

of the flux uncertainty at each epoch (Rodríguez-Pascual et al. 1997, Walsh et al. 2009). These measurements of the variability amplitude are presented in Table 3. Note that F_{var} is often considered as the most reliable parameter of variability because it is accounted for the uncertainty of the flux measurement.

We examined the variability of AGN continuum and H α emission line using the two light curves presented in Section 3. Note that since the flux in the H α light curve, which was measured with the adopted narrow or broad band filter, contains H α emission line flux as well as AGN continuum and non-variable host galaxy contribution. In the case of the continuum light curve, the measured flux is the sum of the flux mainly from AGN continuum and host galaxy (see Figure 3). Thus, the measured variability amplitude depends on the dominance of the AGN component over the host galaxy flux. In other words, even if AGN is highly variable, non-variable host galaxy contribution may dilute the flux variability in the light curve.

The measured R_{max} in the continuum light curve ranges from 1.01 to 1.33, indicating that the maximum

intra-night variability is over 0.3 magnitude, while the highest and the median value of RMS are 0.13 mag and 0.01 mag, respectively. The largest RMS is similar to the median RMS ~ 0.14 mag of typical Seyfert 1 galaxies (Rakshit & Stalin 2017). However, several targets in the sample show very weak variability, leading to relatively low median RMS. If we assume that the measurement error is $\sim 1\%$, continuum flux variability is detected for all targets, with a typical RMS variability $\gtrsim 0.01$ mag. Considering the measurement uncertainty of individual targets, we identified 9 candidates (namely, IDs 5, 27, 29, 30, 32, 35, 36, 38, and 40) as more secure variable targets with a measurable F_{var} of ~ 0.01 - 0.05 mag, which suggests that the detected variability is a few %. The other 11 targets have no measurable F_{var} value, which may be caused by relatively large measurement error compared to the intrinsic variability, dilution due to the dominance of the non-variable host galaxy flux, or the lack of intrinsic AGN variability.

In comparison, the measured R_{max} in the $H\alpha$ light curve ranges from 1.01 to 1.16, while RMS shows a narrower range of ~ 0.01 - 0.06 mag than that of the continuum light curve. The median values of R_{max} , RMS, and F_{var} are 1.04, 0.02 mag, and 0.01 mag, respectively, which is similar to the median values from the continuum light curve. Whereas their highest values are 1.16, 0.06 mag, and 0.02 mag, respectively, showing that the variability of $H\alpha$ is less significant than continuum. As all targets except for ID 31 show RMS $\gtrsim 0.01$ mag, the variability of $H\alpha$ seems detected for most targets. However, after considering the measurement error, we only obtained excess variance for 4 targets (namely, IDs 1, 5, 23 and 30) with $F_{var} \sim 0.01$ - 0.02 mag.

To better understand the measured variability amplitude in the $H\alpha$ light curve, we performed spectral analysis to measure the fraction of the broad $H\alpha$ component in the total flux obtained through each filter. By multiplying the response function of the used filter to the SDSS spectrum of each object, we calculated the fraction of the broad $H\alpha$. Note that the calculated fraction is an upper limit since the adopted aperture of $\sim 9''$ in photometry is much larger than the $\sim 3''$ fiber used for the SDSS spectra. For the broad R filter, the fraction of the broad $H\alpha$ is insignificant ($\lesssim 1\%$), indicating that the detection of the $H\alpha$ variability is very challenging

even if the broad $H\alpha$ emission line intrinsically varies by $< 100\%$. In contrast, the broad $H\alpha$ fraction in the narrow filter is significantly larger (2 – 24%; see last column in Table 3), which is much larger than the measurement uncertainty of 1%. Thus, if the intrinsic variability is significant, it is likely that the variability of $H\alpha$ is detected in the narrow-filter based light curves.

For example, IDs 1, 5, 23, and 30 from MDM observation have considerable $H\alpha$ fraction (14.1%, 1.9%, 4.5%, and 3.5%), and the excess variance is also detected as $F_{var} \sim 1$ -2%. Other targets with no detection of excess variance may have a very small flux ratio of the $H\alpha$ emission or weak variability. Note that for ID 1 and ID 23, we obtained no excess variance F_{var} in the continuum light curve, which is likely due to the fact that non-variable host galaxy component is dominant in the continuum light curve, or that the continuum flux variability amplitude is smaller than the measurement error.

In contrast, the targets observed with broad R filter (namely, IDs 9, 14, 29, 34, 38, and 40) have no measurable F_{var} value due to the insignificant $H\alpha$ fraction. The dominant continuum may have diluted the intrinsic $H\alpha$ variability if any. In the case of ID5 observed with a broad R filter, we obtained somewhat unexpected result. Since the fraction of $H\alpha$ is less than 0.1% in the total flux measured with photometry. the 1% excess variance seems too high to be detected because the $H\alpha$ flux needed to vary by a factor of > 10 . Note that its AGN continuum variability is negligible as we detect no excess variance in the continuum light curve. We consider a possibility that the measurement error in the $H\alpha$ light curve is underestimated and smaller than that of continuum light curve.

In summary, we detected RMS variability of all 20 targets, and obtained excess variance F_{var} for 9 targets based on the observed intra-night continuum light curves. In the case of the $H\alpha$ light curves, we determined RMS variability of $\gtrsim 1\%$ for all targets except for ID 31, and reliable excess variance for 4 targets. Only two candidate, IDs 5 and 30, showed reliable excess variance F_{var} in the light curve of both continuum and $H\alpha$, suggesting that they are the best IMBH candidate in the sample. The other 9 targets, namely, IDs 1, 23, 27, 29, 32, 35, 36, 38, and 40, are also good candidates for further studies since they showed excess variance either in the continuum or $H\alpha$ light curve.

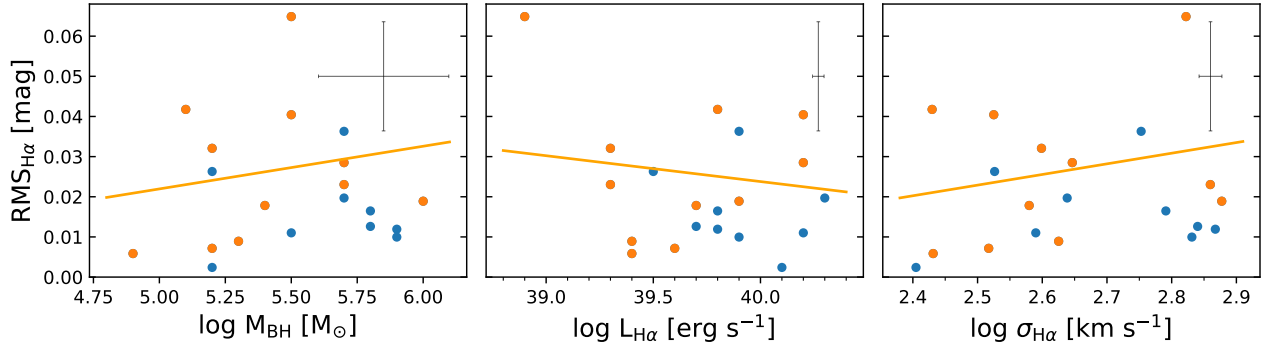


Figure 6. The correlations of $\text{RMS}_{\text{H}\alpha}$ with M_{BH} , $L_{\text{H}\alpha}$, and $\sigma_{\text{H}\alpha}$. The 11 candidates having large variability amplitude selected in Section 4.1 are plotted in orange, and the other candidates with weak variability are plotted in blue. A typical error is shown in the upper right corner. The solid lines show the best linear fit for the 11 variable candidates.

Table 3. Variability information of the observed sample

ID	$\log M_{\text{BH}}$	$\log L_{\text{H}\alpha}$	$(1+z)\tau$	$\sigma_{\text{H}\alpha}$	RMS _{cont.}	$R_{\text{max; cont.}}$	$F_{\text{var; cont.}}$	RMS _{Hα}	$R_{\text{max; H}\alpha}$	$F_{\text{var; H}\alpha}$	Filter_cont	Filter_H α	$f_{\text{H}\alpha}/f_{\text{rot.}}$
(1)	(2)	(3)	(4)	(5)	(6)	(7)	(8)	(9)	(10)	(11)	(12)	(13)	(14)
1	5.5	40.2	2.4	335	0.03	1.08	-	0.04	1.11	0.01	kp1494	kp1517	14.1
3	5.5	40.2	2.4	389	0.01	1.02	-	0.01	1.03	-	kp1494	kp1497	5.1
4	5.7	40.3	2.7	435	0.01	1.02	-	0.02	1.04	-	kp1494	kp1497	10.3
5 ^a	5.7	39.3	0.9	724	< 0.01	1.01	-	0.01	1.02	0.01	V	R	0.1
					0.01	1.02	< 0.01	0.02	1.06	0.02	V	kp1496	1.9
8	5.7	39.9	1.7	566	0.03	1.06	-	0.04	1.10	-	kp1494	kp1497	9.3
9 ^a	5.8	39.8	1.6	618	0.01	1.02	-	0.01	1.02	-	V	R	0.4
					0.01	1.01	-	0.02	1.04	-	V	kp1497	7.3
11	5.8	39.7	1.5	692	0.03	1.08	-	0.01	1.03	-	kp1494	kp1496	6.2
14 ^a	5.9	39.9	1.7	678	0.01	1.04	-	0.01	1.03	-	V	R	0.3
					< 0.01	1.01	-	0.01	1.03	-	V	kp1497	3.5
20	5.9	39.8	1.6	737	0.01	1.04	-	0.01	1.04	-	kp1494	kp1498	4.5
23	6.0	39.9	1.7	754	0.01	1.04	-	0.02	1.05	0.01	kp1494	kp1497	4.5
27	4.9	39.4	1.0	270	0.02	1.05	0.01	0.01	1.02	-	V	kp1497	3.0
29 ^a	5.1	39.8	1.6	269	0.13	1.33	0.02	0.01	1.03	-	V	R	1.4
					0.06	1.15	0.05	0.04	1.10	-	V	kp1498	23.6
30	5.2	39.3	0.9	397	0.03	1.07	0.01	0.03	1.08	0.01	V	kp1496	3.5
31	5.2	40.1	2.1	254	0.01	1.02	-	< 0.01	1.01	-	V	kp1497	6.8
32	5.2	39.6	1.2	329	0.04	1.09	0.02	0.01	1.02	-	V	kp1497	7.6
34 ^a	5.2	39.5	1.1	336	0.04	1.09	-	0.04	1.09	-	V	R	0.6
					0.01	1.02	-	0.03	1.06	-	V	kp1497	11.5
35	5.3	39.4	1.0	422	0.02	1.04	< 0.01	0.01	1.02	-	V	kp1496	3.0
36	5.4	39.7	1.4	380	0.01	1.04	0.01	0.02	1.05	-	V	kp1498	6.8
38 ^a	5.5	38.9	0.6	664	0.04	1.11	0.02	0.02	1.04	-	V	R	0.3
					0.06	1.13	0.05	0.06	1.16	-	V	kp1496	6.2
40 ^a	5.7	40.2	2.3	443	0.01	1.03	-	0.02	1.04	-	V	R	1.1

Table 3 continued

Table 3 (continued)

ID	$\log M_{\text{BH}}$	$\log L_{\text{H}\alpha}$	$(1+z)\tau$	$\sigma_{\text{H}\alpha}$	RMS_{cont}	$R_{\text{max; cont}}$	$F_{\text{var; cont}}$	$\text{RMS}_{\text{H}\alpha}$	$R_{\text{max; H}\alpha}$	$F_{\text{var; H}\alpha}$	Filter_cont	Filter_H α	$f_{\text{H}\alpha}/f_{\text{tot}}$
(1)	(2)	(3)	(4)	(5)	(6)	(7)	(8)	(9)	(10)	(11)	(12)	(13)	(14)
	0.04	1.11	0.04	0.03	1.08	-	V	kp1497	15.3				

NOTE—(1) Identification number assigned in this study. (2) Estimated black hole mass in units of M_{\odot} . (3) Luminosity of the H α broad component in units of erg s^{-1} . (4) Expected time lag in units of days. (5) Velocity dispersion of the H α broad component in units of km s^{-1} . (6) RMS of the continuum part light curve in units of mag. (7) R_{max} of the continuum part light curve. (8) F_{var} of the continuum part light curve in units of mag. (9) RMS of the H α part light curve in units of mag. (10) R_{max} of the H α part light curve. (11) F_{var} of the H α part light curve in units of mag. (12) Filter for the continuum part observation. (13) Filter for the H α part observation. (14) Flux ratio of the broad H α line to the total flux observed with each filter in units of %.

^aObserved at both observation sites.

4.2. Variability vs. AGN properties

We compared the AGN properties and $\text{RMS}_{\text{H}\alpha}$ measured with narrow-filter based light curves (see Figure 6). We computed a least-square linear regression for the highly variable candidates identified in the previous section using `linregress` tool of python `scipy` package (Virtanen et al. 2020). The variability amplitude shows a weak positive correlation with M_{BH} and $\sigma_{\text{H}\alpha}$, whose correlation coefficients (r-value) are 0.19, 0.24 and two sided p-values for a null hypothesis of no correlation are 0.58, 0.48, respectively. On the other hand, $L_{\text{H}\alpha}$ is anti-correlated with the $\text{RMS}_{\text{H}\alpha}$ having weak correlation coefficients (r-value = -0.14 and p-value = 0.67). Similar results have been found by Rakshit & Stalin (2017), who reported that the variability strength has an anti-correlation with AGN luminosity, but a correlation with the M_{BH} and velocity dispersion of the broad permitted lines. The correlation of their sample at $z < 0.2$ is not significant (i.e., p-value > 0.1), suggesting that our result is not inconsistent with that of Rakshit & Stalin (2017). However, the time-based line and the number of epoch are clearly limited, and further studies with sufficient data are required to unveil the nature of the variability correlation of IMBH candidates.

5. DISCUSSION

Several previous studies searched for low mass BHs hosted in the dwarf galaxies by detecting the spectral signature of BH accretion using the SDSS galaxy sample, and identified IMBH candidates with broad $\text{H}\alpha$ emission line (e.g., Reines et al. 2013; Baldassare et al. 2015; Eun et al. 2017; Chilingarian et al. 2018). We compared the selection criteria and the results of the previous works with this study. For example, Eun et al. (2017) found 611 broad $\text{H}\alpha$ candidates from SDSS DR7 data. Their mean value of $\text{H}\alpha$ luminosity ($10^{40.7 \pm 0.3}$ erg s^{-1}) is larger than the mean value of our sample of 131 objects with a broad $\text{H}\alpha$ ($10^{40.3}$ erg s^{-1}). Velocity dispersion of $\text{H}\alpha$ of most of their targets is also larger than 1000 km s^{-1} (see Figure 10 in Eun et al. 2017), while $\sim 70\%$ of our broad $\text{H}\alpha$ candidates (92/131) has $\sigma_{\text{H}\alpha}$ smaller than 1000 km s^{-1} . Consequently, the estimated M_{BH} of the sample in Eun et al. (2017) is larger than $10^6 M_{\odot}$. In contrast, we have found 25 targets whose estimated M_{BH} is less than $10^6 M_{\odot}$. Note that Eun et al. (2017) conservatively selected clear type 1 AGN candidates in order to avoid the false detection. In contrast, we set the lower $\sigma_{\text{H}\alpha}$ cut for the definition of the type 1 AGN, and performed more delicate spectral analysis using χ^2_{red} and BIC to find the targets with the weak $\text{H}\alpha$ broad component.

Similar comparison can be done with the broad $\text{H}\alpha$ candidates from Reines et al. (2013). They have identified the candidates with dimmer $\text{H}\alpha$ broad component than ours as their mean $L_{\text{H}\alpha}$ ($10^{39.7}$ erg s^{-1}) is lower than that of our 131 broad $\text{H}\alpha$ candidates (i.e., $10^{40.3}$ erg s^{-1}). Also, their mean $\sigma_{\text{H}\alpha}$ (~ 670 km s^{-1}) is lower than ours (~ 870 km s^{-1}). The main difference comes from the fact that they only surveyed dwarf galaxies at $z < 0.055$, by imposing stellar mass limit, i.e., $< 3 \times 10^9 M_{\odot}$. Since we searched more distant targets, it is likely that we missed the candidates having a weak $\text{H}\alpha$ broad component at $z > 0.055$. Note that among the 25 IMBH candidates in this study, whose M_{BH} is less than $10^6 M_{\odot}$, only one target is overlapped with the IMBH candidates in Reines et al. (2013). While both samples were selected from the SDSS catalog based on similar selection criteria, the details of the selection scheme and the spectral decomposition analysis caused the difference. It shows that more missing IMBH candidates can be identified among SDSS galaxies by refining the selection procedures.

Chilingarian et al. (2018) also performed a similar study to identify IMBHs among SDSS galaxies. They reported IMBH candidates whose estimated M_{BH} is less than $10^5 M_{\odot}$ based on their own non-parametric emission line fitting method along with X-ray flux analysis (Chilingarian et al. 2017). While it is possible that for some of the candidates, their fitting method constructing multiple template sets of flux-normalized Gaussians may suffer an overfitting problem, underestimating the luminosity and velocity dispersion of the broad $\text{H}\alpha$ component, they demonstrated that spectral analysis can be utilized to find IMBH candidates even with $M_{\text{BH}} \sim 10^4 M_{\odot}$.

The presence of a broad $\text{H}\alpha$ may not be sufficient to be qualified as type 1 AGN since the line width of $\text{H}\alpha$ of IMBH candidates is relatively narrow compared to the conventional limit of $\sim 1,000$ km s^{-1} , and other sources such as supernovae are able to exhibit a broad $\text{H}\alpha$ (e.g., Izotov et al. 2007; Izotov & Thuan 2009b; Graur & Maoz 2013). However, by detecting variability, these targets can be confirmed as mass accreting IMBHs. While various studies performed variability analysis over a relatively long time scale for identifying IMBH candidates (e.g., Baldassare et al. 2018; Martínez-Palomera et al. 2020), Short-time scale, i.e., intra-night variability studies are rare. We compare our results with the intra-night variability analysis conducted by Kim et al. (2018), who monitored AGN candidates in the SMBH regime. While the FOV ($\sim 10' \times 10'$) of our photometric observations is much smaller and the time baseline is shorter (i.e., ~ 8 hours) than those of Kim et al. (2018), we obtained

measurable variability amplitudes for a subsample of the IMBH candidates, suggesting that it is possible to detect variability of IMBH candidates based on intra-night monitoring programs with a relatively short cadence. Future narrow-band monitoring programs with well defined strategies on the time base line and cadence can provide valuable assessment and confirmation of IMBH candidates.

6. SUMMARY AND CONCLUSION

To detect the accretion signature of IMBH candidates, we identified the galaxies with a broad H α emission line, and performed further analysis to constrain the nature of these targets. The main results are summarized as follows.

- We performed spectral analysis in the H α emission line region using a large sample of the SDSS DR7 galaxy, and newly found 131 targets with a weak broad H α line. Among them, 25 targets have M_{BH} less than $10^6 M_{\odot}$.
- To find additional evidence of AGN, we obtained X-ray data and measured X-ray luminosity for 19

candidates. However the estimated M_{BH} of these targets is larger than $10^6 M_{\odot}$.

- We observed 20 IMBH candidates for an intra-night variability test and reported 11 objects with the largest variability amplitude as the best IMBH candidates.

Our study demonstrated that an intensive monitoring campaign with a larger-aperture telescope along with a narrow-band filter can provide strong constraints over the population of IMBHs at low z , by overcoming the relatively large measurement error and the limited number of epochs of this study. The best IMBH candidates obtained in this study are one of the best suitable targets for further studies, i.e., spectroscopic reverberation mapping, to confirm them as IMBHs and determine reliable black hole masses.

ACKNOWLEDGMENTS

This work was supported by the National Research Foundation of Korea grant funded by the Korean government (NRF-2021R1A2C3008486).

REFERENCES

- Abazajian, K. N., Adelman-McCarthy, J. K., Agüeros, M. A., et al. 2009, *ApJS*, 182, 543, doi: [10.1088/0067-0049/182/2/543](https://doi.org/10.1088/0067-0049/182/2/543)
- Abbott, R., Abbott, T. D., Abraham, S., et al. 2020, *Phys. Rev. Lett.*, 125, 101102, doi: [10.1103/PhysRevLett.125.101102](https://doi.org/10.1103/PhysRevLett.125.101102)
- Aranzana, E., Körtling, E., Uttley, P., Scaringi, S., & Bloemen, S. 2018, *MNRAS*, 476, 2501, doi: [10.1093/mnras/sty413](https://doi.org/10.1093/mnras/sty413)
- Astropy Collaboration, Robitaille, T. P., Tollerud, E. J., et al. 2013, *A&A*, 558, A33, doi: [10.1051/0004-6361/201322068](https://doi.org/10.1051/0004-6361/201322068)
- Astropy Collaboration, Price-Whelan, A. M., Sipőcz, B. M., et al. 2018, *AJ*, 156, 123, doi: [10.3847/1538-3881/aabc4f](https://doi.org/10.3847/1538-3881/aabc4f)
- Bañados, E., Venemans, B. P., Mazzucchelli, C., et al. 2018, *Nature*, 553, 473, doi: [10.1038/nature25180](https://doi.org/10.1038/nature25180)
- Bae, H.-J., & Woo, J.-H. 2014, *ApJ*, 795, 30, doi: [10.1088/0004-637X/795/1/30](https://doi.org/10.1088/0004-637X/795/1/30)
- Baldassare, V. F., Geha, M., & Greene, J. 2018, *ApJ*, 868, 152, doi: [10.3847/1538-4357/aae6cf](https://doi.org/10.3847/1538-4357/aae6cf)
- Baldassare, V. F., Reines, A. E., Gallo, E., & Greene, J. E. 2015, *ApJL*, 809, L14, doi: [10.1088/2041-8205/809/1/L14](https://doi.org/10.1088/2041-8205/809/1/L14)
- Baumgardt, H. 2017, *MNRAS*, 464, 2174, doi: [10.1093/mnras/stw2488](https://doi.org/10.1093/mnras/stw2488)
- Bentz, M. C., Denney, K. D., Grier, C. J., et al. 2013, *ApJ*, 767, 149, doi: [10.1088/0004-637X/767/2/149](https://doi.org/10.1088/0004-637X/767/2/149)
- Bertin, E., & Arnouts, S. 1996, *A&AS*, 117, 393, doi: [10.1051/aas:1996164](https://doi.org/10.1051/aas:1996164)
- Bertin, E., Mellier, Y., Radovich, M., et al. 2002, in *Astronomical Society of the Pacific Conference Series*, Vol. 281, *Astronomical Data Analysis Software and Systems XI*, ed. D. A. Bohlender, D. Durand, & T. H. Handley, 228
- Cappellari, M., & Emsellem, E. 2004, *PASP*, 116, 138, doi: [10.1086/381875](https://doi.org/10.1086/381875)
- Chilingarian, I. V., Katkov, I. Y., Zolotukhin, I. Y., et al. 2018, *ApJ*, 863, 1, doi: [10.3847/1538-4357/aad184](https://doi.org/10.3847/1538-4357/aad184)
- Chilingarian, I. V., Zolotukhin, I. Y., Katkov, I. Y., et al. 2017, *ApJS*, 228, 14, doi: [10.3847/1538-4365/228/2/14](https://doi.org/10.3847/1538-4365/228/2/14)
- Cseh, D., Webb, N. A., Godet, O., et al. 2015, *MNRAS*, 446, 3268, doi: [10.1093/mnras/stu2363](https://doi.org/10.1093/mnras/stu2363)
- Dong, X.-B., Ho, L. C., Yuan, W., et al. 2012, *ApJ*, 755, 167, doi: [10.1088/0004-637X/755/2/167](https://doi.org/10.1088/0004-637X/755/2/167)
- Elvis, M., Maccacaro, T., Wilson, A. S., et al. 1978, *MNRAS*, 183, 129, doi: [10.1093/mnras/183.2.129](https://doi.org/10.1093/mnras/183.2.129)
- Eun, D.-i., Woo, J.-H., & Bae, H.-J. 2017, *ApJ*, 842, 5, doi: [10.3847/1538-4357/aa6daf](https://doi.org/10.3847/1538-4357/aa6daf)

- Filippenko, A. V., & Ho, L. C. 2003, *ApJL*, 588, L13, doi: [10.1086/375361](https://doi.org/10.1086/375361)
- Gebhardt, K., Pryor, C., O'Connell, R. D., Williams, T. B., & Hesser, J. E. 2000, *AJ*, 119, 1268, doi: [10.1086/301275](https://doi.org/10.1086/301275)
- Gerssen, J., van der Marel, R. P., Gebhardt, K., et al. 2002, *AJ*, 124, 3270, doi: [10.1086/344584](https://doi.org/10.1086/344584)
- Graur, O., & Maoz, D. 2013, *MNRAS*, 430, 1746, doi: [10.1093/mnras/sts718](https://doi.org/10.1093/mnras/sts718)
- Greene, J. E. 2012, *Nature Communications*, 3, 1304, doi: [10.1038/ncomms2314](https://doi.org/10.1038/ncomms2314)
- Greene, J. E., & Ho, L. C. 2004, *ApJ*, 610, 722, doi: [10.1086/421719](https://doi.org/10.1086/421719)
- . 2005, *ApJ*, 630, 122, doi: [10.1086/431897](https://doi.org/10.1086/431897)
- . 2007, *ApJ*, 670, 92, doi: [10.1086/522082](https://doi.org/10.1086/522082)
- Greene, J. E., Strader, J., & Ho, L. C. 2020, *ARA&A*, 58, 257, doi: [10.1146/annurev-astro-032620-021835](https://doi.org/10.1146/annurev-astro-032620-021835)
- Izotov, Y. I., & Thuan, T. X. 2007, *ApJ*, 665, 1115, doi: [10.1086/519922](https://doi.org/10.1086/519922)
- . 2009a, *ApJ*, 690, 1797, doi: [10.1088/0004-637X/690/2/1797](https://doi.org/10.1088/0004-637X/690/2/1797)
- . 2009b, *ApJ*, 707, 1560, doi: [10.1088/0004-637X/707/2/1560](https://doi.org/10.1088/0004-637X/707/2/1560)
- Izotov, Y. I., Thuan, T. X., & Guseva, N. G. 2007, *ApJ*, 671, 1297, doi: [10.1086/522923](https://doi.org/10.1086/522923)
- Kass, R. E., & Raftery, A. E. 1995, *J. Am. Stat. Assoc.*, 90, 773, doi: [10.2307/2291091](https://doi.org/10.2307/2291091)
- Kauffmann, G., Heckman, T. M., Tremonti, C., et al. 2003, *MNRAS*, 346, 1055, doi: [10.1111/j.1365-2966.2003.07154.x](https://doi.org/10.1111/j.1365-2966.2003.07154.x)
- Kim, J., Karouzos, M., Im, M., et al. 2018, *Journal of Korean Astronomical Society*, 51, 89, doi: [10.5303/JKAS.2018.51.4.89](https://doi.org/10.5303/JKAS.2018.51.4.89)
- Kormendy, J., & Ho, L. C. 2013, *ARA&A*, 51, 511, doi: [10.1146/annurev-astro-082708-101811](https://doi.org/10.1146/annurev-astro-082708-101811)
- Kormendy, J., & Richstone, D. 1995, *ARA&A*, 33, 581, doi: [10.1146/annurev.aa.33.090195.003053](https://doi.org/10.1146/annurev.aa.33.090195.003053)
- Lang, D., Hogg, D. W., Mierle, K., Blanton, M., & Roweis, S. 2010, *AJ*, 139, 1782, doi: [10.1088/0004-6256/139/5/1782](https://doi.org/10.1088/0004-6256/139/5/1782)
- Latif, M. A., Schleicher, D. R. G., Schmidt, W., & Niemeyer, J. C. 2013, *MNRAS*, 436, 2989, doi: [10.1093/mnras/stt1786](https://doi.org/10.1093/mnras/stt1786)
- Le, H. A. N., Woo, J.-H., & Xue, Y. 2020, *ApJ*, 901, 35, doi: [10.3847/1538-4357/abada0](https://doi.org/10.3847/1538-4357/abada0)
- Liu, H.-Y., Yuan, W., Dong, X.-B., Zhou, H., & Liu, W.-J. 2018, *ApJS*, 235, 40, doi: [10.3847/1538-4365/aab88e](https://doi.org/10.3847/1538-4365/aab88e)
- Loeb, A., & Rasio, F. A. 1994, *ApJ*, 432, 52, doi: [10.1086/174548](https://doi.org/10.1086/174548)
- Martínez-Palomera, J., Lira, P., Bhalla-Ladd, I., Förster, F., & Plotkin, R. M. 2020, *ApJ*, 889, 113, doi: [10.3847/1538-4357/ab5f5b](https://doi.org/10.3847/1538-4357/ab5f5b)
- McConnell, N. J., & Ma, C.-P. 2013, *ApJ*, 764, 184, doi: [10.1088/0004-637X/764/2/184](https://doi.org/10.1088/0004-637X/764/2/184)
- Mezcua, M. 2017, *International Journal of Modern Physics D*, 26, 1730021, doi: [10.1142/S021827181730021X](https://doi.org/10.1142/S021827181730021X)
- Miller, J. M., Fabbiano, G., Miller, M. C., & Fabian, A. C. 2003, *ApJL*, 585, L37, doi: [10.1086/368373](https://doi.org/10.1086/368373)
- Mortlock, D. J., Warren, S. J., Venemans, B. P., et al. 2011, *Nature*, 474, 616, doi: [10.1038/nature10159](https://doi.org/10.1038/nature10159)
- Mushotzky, R. F., Edelson, R., Baumgartner, W., & Gandhi, P. 2011, *ApJL*, 743, L12, doi: [10.1088/2041-8205/743/1/L12](https://doi.org/10.1088/2041-8205/743/1/L12)
- Nucita, A. A., Manni, L., De Paolis, F., Giordano, M., & Ingrosso, G. 2017, *ApJ*, 837, 66, doi: [10.3847/1538-4357/aa5f4f](https://doi.org/10.3847/1538-4357/aa5f4f)
- Onoue, M., Kashikawa, N., Matsuoka, Y., et al. 2019, *ApJ*, 880, 77, doi: [10.3847/1538-4357/ab29e9](https://doi.org/10.3847/1538-4357/ab29e9)
- Park, D., Woo, J.-H., Treu, T., et al. 2012, *ApJ*, 747, 30, doi: [10.1088/0004-637X/747/1/30](https://doi.org/10.1088/0004-637X/747/1/30)
- Peterson, B. M. 1993, *PASP*, 105, 247, doi: [10.1086/133140](https://doi.org/10.1086/133140)
- Peterson, B. M., Ferrarese, L., Gilbert, K. M., et al. 2004, *ApJ*, 613, 682, doi: [10.1086/423269](https://doi.org/10.1086/423269)
- Pooley, D., & Rappaport, S. 2006, *ApJL*, 644, L45, doi: [10.1086/505344](https://doi.org/10.1086/505344)
- Rakshit, S., & Stalin, C. S. 2017, *ApJ*, 842, 96, doi: [10.3847/1538-4357/aa72f4](https://doi.org/10.3847/1538-4357/aa72f4)
- Rakshit, S., Woo, J.-H., Gallo, E., et al. 2019, *ApJ*, 886, 93, doi: [10.3847/1538-4357/ab49fd](https://doi.org/10.3847/1538-4357/ab49fd)
- Reines, A. E., & Comastri, A. 2016, *PASA*, 33, e054, doi: [10.1017/pasa.2016.46](https://doi.org/10.1017/pasa.2016.46)
- Reines, A. E., Greene, J. E., & Geha, M. 2013, *ApJ*, 775, 116, doi: [10.1088/0004-637X/775/2/116](https://doi.org/10.1088/0004-637X/775/2/116)
- Remillard, R. A., & McClintock, J. E. 2006, *ARA&A*, 44, 49, doi: [10.1146/annurev.astro.44.051905.092532](https://doi.org/10.1146/annurev.astro.44.051905.092532)
- Rodríguez-Pascual, P. M., Alloin, D., Clavel, J., et al. 1997, *ApJS*, 110, 9, doi: [10.1086/312996](https://doi.org/10.1086/312996)
- Sánchez-Blázquez, P., Peletier, R. F., Jiménez-Vicente, J., et al. 2006, *MNRAS*, 371, 703, doi: [10.1111/j.1365-2966.2006.10699.x](https://doi.org/10.1111/j.1365-2966.2006.10699.x)
- Shen, Y., & Liu, X. 2012, *ApJ*, 753, 125, doi: [10.1088/0004-637X/753/2/125](https://doi.org/10.1088/0004-637X/753/2/125)
- Silk, J., & Arons, J. 1975, *ApJL*, 200, L131, doi: [10.1086/181914](https://doi.org/10.1086/181914)
- Sutton, A. D., Roberts, T. P., Walton, D. J., Gladstone, J. C., & Scott, A. E. 2012, *MNRAS*, 423, 1154, doi: [10.1111/j.1365-2966.2012.20944.x](https://doi.org/10.1111/j.1365-2966.2012.20944.x)
- Thompson, T. A., Kochanek, C. S., Stanek, K. Z., et al. 2019, *Science*, 366, 637, doi: [10.1126/science.aau4005](https://doi.org/10.1126/science.aau4005)

- Tody, D. 1986, in Society of Photo-Optical Instrumentation Engineers (SPIE) Conference Series, Vol. 627, Instrumentation in astronomy VI, ed. D. L. Crawford, 733, doi: [10.1117/12.968154](https://doi.org/10.1117/12.968154)
- Tremonti, C. A., Heckman, T. M., Kauffmann, G., et al. 2004, ApJ, 613, 898, doi: [10.1086/423264](https://doi.org/10.1086/423264)
- van Dokkum, P. G. 2001, PASP, 113, 1420, doi: [10.1086/323894](https://doi.org/10.1086/323894)
- Vanden Berk, D. E., Shen, J., Yip, C.-W., et al. 2006, AJ, 131, 84, doi: [10.1086/497973](https://doi.org/10.1086/497973)
- Virtanen, P., Gommers, R., Oliphant, T. E., et al. 2020, Nature Methods, 17, 261, doi: [10.1038/s41592-019-0686-2](https://doi.org/10.1038/s41592-019-0686-2)
- Volonteri, M., Lodato, G., & Natarajan, P. 2008, MNRAS, 383, 1079, doi: [10.1111/j.1365-2966.2007.12589.x](https://doi.org/10.1111/j.1365-2966.2007.12589.x)
- Walsh, J. L., Minezaki, T., Bentz, M. C., et al. 2009, ApJS, 185, 156, doi: [10.1088/0067-0049/185/1/156](https://doi.org/10.1088/0067-0049/185/1/156)
- Webb, N., Cseh, D., Lenc, E., et al. 2012, Science, 337, 554, doi: [10.1126/science.1222779](https://doi.org/10.1126/science.1222779)
- Woo, J.-H., Bae, H.-J., Son, D., & Karouzos, M. 2016, ApJ, 817, 108, doi: [10.3847/0004-637X/817/2/108](https://doi.org/10.3847/0004-637X/817/2/108)
- Woo, J.-H., Cho, H., Gallo, E., et al. 2019a, Nature Astronomy, 3, 755, doi: [10.1038/s41550-019-0790-3](https://doi.org/10.1038/s41550-019-0790-3)
- Woo, J.-H., Kim, J.-G., Park, D., et al. 2014, Journal of Korean Astronomical Society, 47, 167, doi: [10.5303/JKAS.2014.47.5.167](https://doi.org/10.5303/JKAS.2014.47.5.167)
- Woo, J.-H., & Urry, C. M. 2002, ApJ, 579, 530, doi: [10.1086/342878](https://doi.org/10.1086/342878)
- Woo, J.-H., Yoon, Y., Park, S., Park, D., & Kim, S. C. 2015, ApJ, 801, 38, doi: [10.1088/0004-637X/801/1/38](https://doi.org/10.1088/0004-637X/801/1/38)
- Woo, J.-H., Son, D., Gallo, E., et al. 2019b, Journal of Korean Astronomical Society, 52, 109, doi: [10.5303/JKAS.2019.52.4.109](https://doi.org/10.5303/JKAS.2019.52.4.109)

APPENDIX

We present the spectral decomposition results of the 24 broad $H\alpha$ candidates with $M_{\text{BH}} < 10^6 M_{\odot}$ in Figure 7. The result of candidate 1 is shown in Figure 1. As explain in Section 2.2.1, IDs 2, 12, 14, 16, 20, 23, and 24 show the case that the model without $H\alpha$ broad component (second and forth column) cannot fit the $H\alpha$ line well and large residual is present between each emission line. The model without $H\alpha$ broad component for IDs 3, 5, and 17 is not able to fit the both $H\alpha$ and [SII] lines, and the model for the other candidates cannot fit the [SII] lines appropriately. They fit the [SII] lines much broader than the real, so a significant residual is shown between the two [SII] lines. The amplitude of $H\alpha$ broad component of the IDs 6, 12, 14, and 20 seems low relative to the amplitude of the emission lines. However their absolute amplitude is larger than their flux density error and the residual around the emission lines, so adding the $H\alpha$ broad component is reliable. Also note that, according the criteria of Section 2.2.1, the BIC and χ_{red}^2 of their fitting results decrease by 10 when the broad component is added, and the A/N of each broad component is larger than 10.

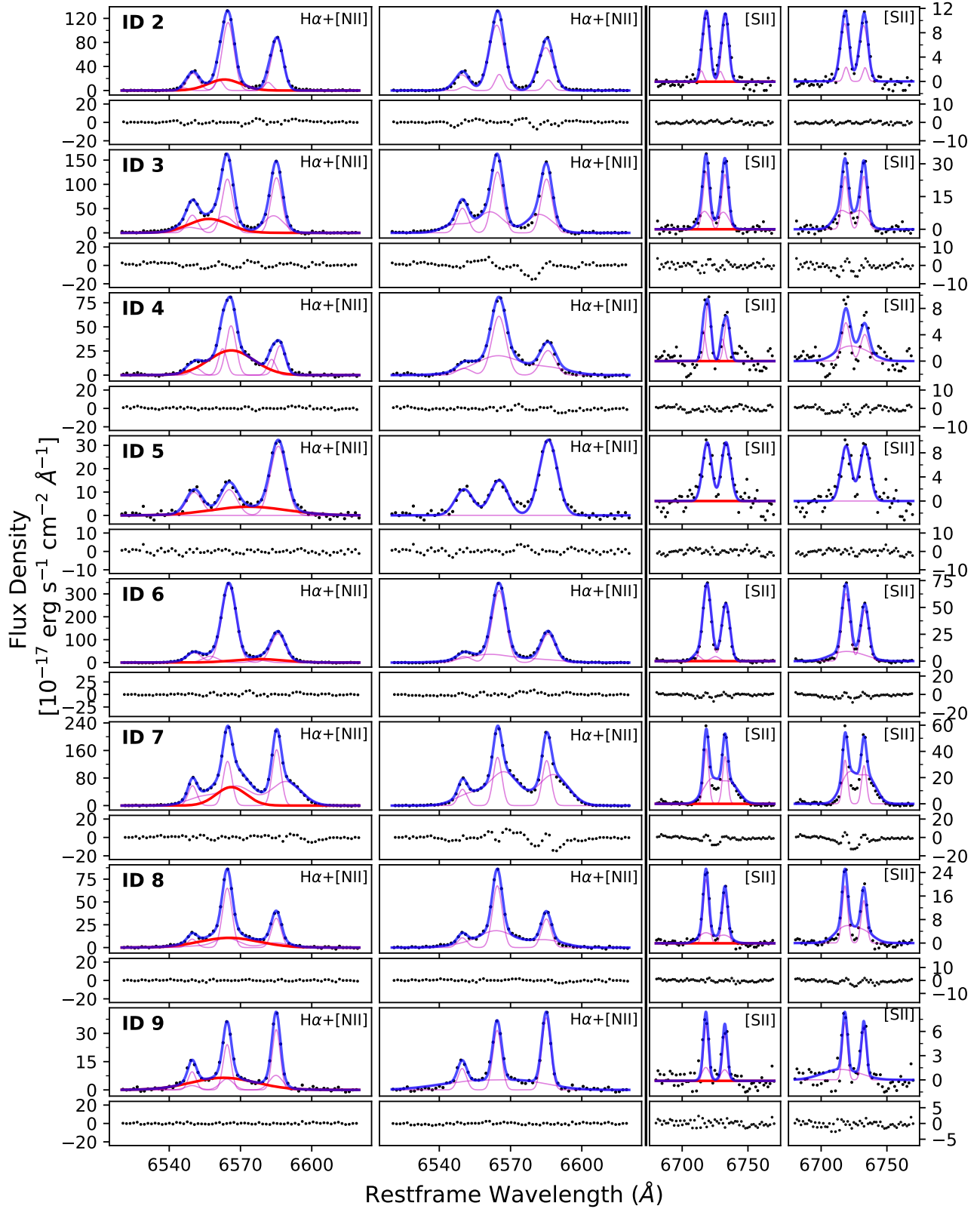


Figure 7. Spectral decomposition of the 24 broad H α candidate whose estimated M_{BH} is smaller than $10^6 M_{\odot}$. The first and third column show the best fit model with H α broad component for each emission line region. The second and fourth column show the best fit model without H α broad component. The stellar continuum subtracted spectrum is plotted black, and the blue line shows the best fit model composed of narrow Gaussian components (magenta) and H α broad component (red). At the bottom of each panel, the residuals between the spectrum and the best fit model are plotted in black.

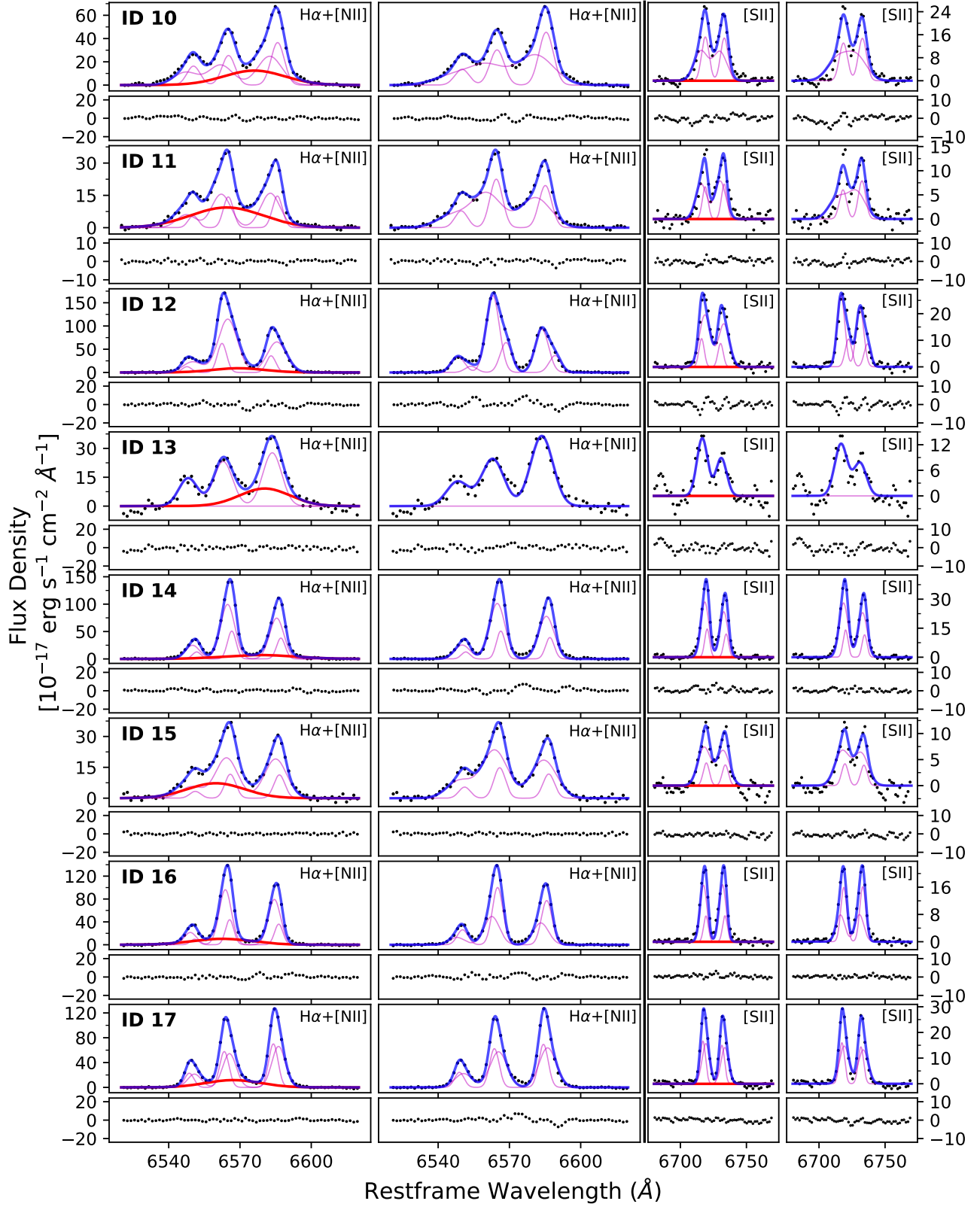


Figure 7. Continued

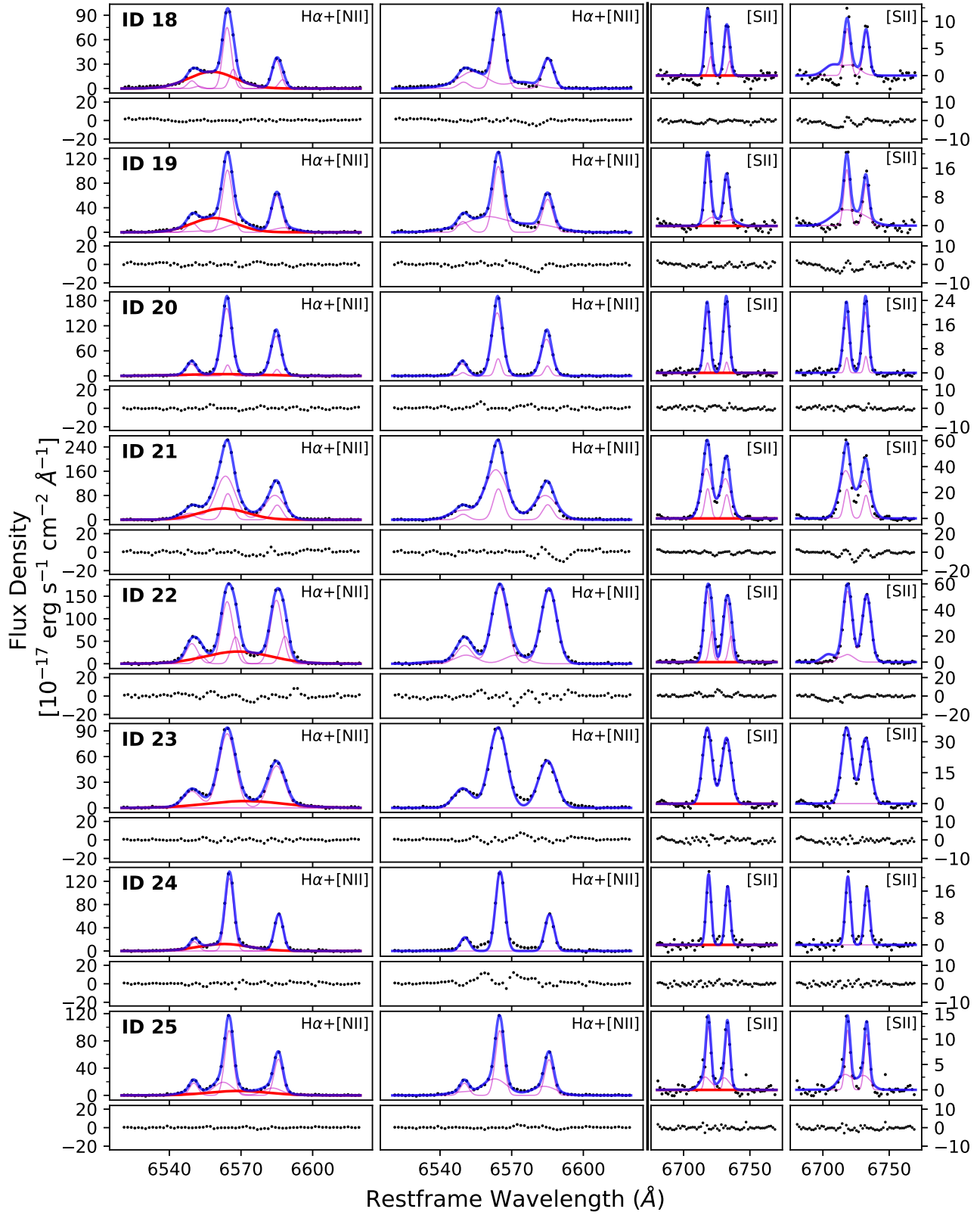


Figure 7. Continued